Nanoscale

COMMUNICATION

View Article Online
View Journal | View Issue

Check for updates

Cite this: *Nanoscale*, 2025, **17**, 14597

Received 20th March 2025,
Accepted 23rd May 2025

DOI: 10.1039/d5nr01160d

rsc.li/nanoscale

Published on 27 2568. Downloaded on 4/2/2569 17:04:26.

Operando characterization of lithium battery internal temperatures *via* upconverting nanoparticle thermometry†

Fei Hu, ‡[a] Ziyang Ye, ‡[b] Andrea D. Pickel *[b,c] and Wyatt E. Tenhaeff *[a,b]

Charging lithium batteries at high rates requires reliable, accurate temperature characterization for battery safety. Monitoring the external temperature of battery packaging does not provide satisfactory insight into thermal processes within the cell, especially at high rates when significant temperature gradients can develop. For *operando* characterization of the internal temperatures of Li batteries, a novel thermometry technique based on the luminescence of upconverting nanoparticles (UCNPs) was demonstrated. $NaYF_4$:Yb^{3+},Er^{3+} UCNPs with an average diameter of 27 nm were introduced onto the surface of battery cell components (anode, cathode, and separator) and shown to have negligible adverse effects on the cell's performance, while enabling *operando* temperature measurements of all three components in a single cell. With application of a discharge current of 65 mA in a commercial primary coin cell (CR2032), a maximum temperature difference of 7.9 °C was measured between the cell separator and external packaging. It is envisioned that this technique can be extended to larger format lithium-ion battery cells, revealing non-uniform internal temperature distribution within the cells to better understand critical thermal processes.

1. Introduction

The electrification of transportation (*e.g.*, electric vehicles) has driven incredible demand for Li batteries, especially those possessing high rate capabilities (fast charging).[1,2] However, fast-charging of Li batteries poses significant safety concerns associated with overheating and subsequent gas release and even combustion.[3–5] To evaluate battery health/safety and prevent thermal runaways that lead to catastrophic battery fires, temperature measurement and thermal management of Li batteries is critical. The simplest approach to monitoring Li battery temperatures is *via* external measurement of the battery packaging – by attaching a thermal sensor directly to the battery, for example. But, it is the internal battery temperature that dictates battery failure and hazardous thermal processes; thus, *in situ* characterization of internal temperatures within lithium ion batteries is necessary and worthy of deep investigation.[5–7] The internal temperature is challenging to predict due to the poorly studied thermal conductivity of components in batteries. Furthermore, thermal contact resistance has been reported to dominate the total battery thermal resistance and be influenced by the state of charge and presence of electrolytes.[8] All these factors complicate the prediction of the internal temperature of lithium batteries *via* external temperature measurements. In addition, microscale hot spots in batteries introduced by laser heating have been reported to cause Li leaching, but a suitable method for quantifying the internal local temperature is still missing.[9]

Probing internal temperatures of Li batteries is challenging because the cells must be completely sealed to avoid moisture contamination and contain the volatile electrolyte. Several recent studies and review articles describe how *operando* temperature characterization of lithium batteries has been achieved, along with the principles of the temperature measurement and necessary modifications to the electrochemical cell.[5–7,10–13] The most common approach is to insert a thermal sensor (*e.g.*, thermocouple, resistance temperature detector (RTD), *etc.*) through the battery packaging, then seal the penetration externally.[14–19] When inserted between the electrodes, these sensors will inevitably disrupt the electrical and thermal gradients within the battery. The macroscopic length scale of these sensors (typically >1 mm^2 in area and >100 μm in thickness) can obscure a significant fraction of the electrochemically active area and widen the electrode spacing, leading to performance (power) degradation.[5,6] Also, this mis-

[a]*Department of Chemical Engineering, University of Rochester, Rochester, New York 14627, USA. E-mail: wyatt.tenhaeff@rochester.edu*
[b]*Materials Science Program, University of Rochester, Rochester, New York 14627, USA. E-mail: apickel@ur.rochester.edu*
[c]*Department of Mechanical Engineering, University of Rochester, Rochester, New York 14627, USA*

†Electronic supplementary information (ESI) available. See DOI: https://doi.org/10.1039/d5nr01160d

‡These authors contributed equally.

Published on 27 2568. Downloaded on 4/2/2569 17:04:26.

match in length scales makes it difficult to spatially resolve the temperatures of individual cell components. Other common insertable sensors are based on optical fiber probes incorporating Rayleigh or Bragg-grating sensors.[19–21] The accuracy of these sensors can be compromised due to their sensitivity to mechanical strain, requiring multiple sensors or special cell designs to isolate potential interferences.[10,22] Both the conventional thermal sensor and optical fiber probes provide good temporal resolution (seconds), but the characteristic size of these probes (tens to hundreds of micrometers) relative to the length scale of the electrode separation (15–20 μm) makes it difficult to spatially resolve temperatures within the cell. The increased electrode separation due to the sensors has also been shown to significantly influence lithiation kinetics at high currents.[23]

Alternatively, ultrasonic techniques, X-ray diffraction (XRD), Raman spectroscopy, and impedance spectroscopy-based techniques can provide non-contact characterization of internal temperatures. For ultrasonic techniques, individual temperatures of different battery components cannot be resolved.[24] XRD and Raman thermometry are limited to specific probe materials within the electrochemical cell and cannot be applied universally to all cell components.[25–28] XRD-based thermometry, utilizing high brilliance synchrotron sources, has been applied to Cu and Al current collectors, wherein the temperature is determined from the thermally-induced strain of the crystalline lattice.[25,26] Apart from thermal strain, mechanical strain caused by (de)lithiation of electrodes can lead to lattice parameter deviations, complicating the temperature analysis.[26] Similarly, Raman spectroscopy focuses on the temperature dependence of vibrational modes in Raman-active materials (*e.g.*, silicon, carbon nanostructures, graphene, *etc.*) – requiring the inclusion of these materials in the electrochemical cell.[27,29,30] The Raman-active modes should also be insensitive to Li (de)insertion to eliminate electrochemical interferences, further limiting the breadth of feasible materials. Temperature monitoring through electrochemical impedance spectroscopy is compelling because it can be performed on fully-assembled, practical cells without complex, costly instrumentation (doesn't require redesign of the cell to accommodate the measurement). However, impedance analysis (1) can disrupt the electrochemical processes during galvanostatic operation and (2) is convoluted with other processes (*e.g.*, electrode capacity fade, irreversible interfacial chemical reactions, and electrolyte decomposition).[31–34] Another challenge inherent to these three techniques is their long data acquisition time when applied in batteries (tens of seconds to minutes), precluding fine temporal resolution of temperature.[27] A non- or less-destructive *operando* temperature measurement technique that can temporally and spatially resolve temperatures universally across all cell components is needed to better understand thermal processes within Li batteries. Optical spectroscopy methods have proven powerful for *operando* characterization of other non-thermal battery parameters, including structural evolution and electrochemical activity, motivating the present work.[35]

Herein, a nanothermometry technique based on upconverting nanoparticles (UCNPs) to probe the internal temperature of Li batteries is demonstrated. This technique relies on acquiring and analyzing the temperature-sensitive spectral peak intensity ratio of the emitted green light spectrum from UCNPs irradiated with near-infrared light. Compared to previous approaches using optical fibers embedded with UCNPs,[36–38] directly depositing UCNPs onto the internal components of lithium batteries eliminates limitations associated with inserted sensors, such as altered local lithiation mechanisms and kinetic changes caused by the presence of sensors hundreds of microns in size.[23] Furthermore, here we excite and collect the emission through an objective lens to achieve sub-micrometer spatial resolution, far surpassing the resolution achievable with optical fibers. The nanoscale dimensions of the UCNPs do not alter the electrode spacing or cell dimensions, allowing for the baseline battery performance of the cells to be maintained. Moreover, the UCNPs are chemically inert within the electrochemical cell, which allows high concentrations to be incorporated without detrimental side reactions. These high concentrations directly lead to high signal-to-noise in the collected UCNP emission, allowing the conversion of luminescence spectra to internal temperature with fast acquisition (second level) time and relatively low laser intensity. Most importantly, spatially resolved *operando* characterization (sub-micrometer level) of each individual component within the electrochemical cells is feasible, providing critical insights for battery thermal engineering.

2. Experimental

2.1 Preparation of customized coin cells

Coin cells (CR2032) were modified with a Kapton® film window, and the edges were sealed by epoxy (LOCTITE® EA E-30CL). The optical window on the cell is 5/16-inch (0.79 cm) diameter. To create optical pathways for the laser, holes in the separator (1/16 inch (0.16 cm)) and Li anode (1/8 inch (0.32 cm)) were punched using a steel hand punch. 3 μl $NaYF_4$ doped with Yb^{3+} and Er^{3+} upconverting nanoparticles (UCNP) in cyclohexane solution (20 mg ml^{-1}, CD Bioparticles) was added onto the surface of NMC532 cathode, MnO_2 cathode, Celgard®/glass fiber separator and Li anode surface, followed by vacuum drying overnight at 85 °C to eliminate residual solvent. Liquid electrolyte was 1 M lithium hexafluorophosphate ($LiPF_6$) in ethylene carbonate/dimethyl carbonate/diethyl carbonate (EC/DMC/DEC, 1 : 1 : 1 by volume, (Sigma Aldrich) with a volume of 75 μl for NMC532-Li cells and 100 μl for MnO_2-Li cells.

2.2 NMC532-Li coin cells for cycling

Single-sided $LiNi_{0.5}Mn_{0.3}Co_{0.2}O_2$ (NMC532, provided by Argonne National Laboratory, with a mass loading of 90 wt% active materials: 10.12 mg cm^{-2}, areal capacity = 1.6 mA h cm^{-2}, diameter = 9/16 inch (14 mm), thickness = 62 μm) was used as working electrode, and Li foil (Sigma Aldrich) was

 This journal is © The Royal Society of Chemistry 2025

Published on 27 2568. Downloaded on 4/2/2569 17:04:26.

employed as the counter electrode (diameter = 5/8 inch (16 mm)), two of which were separated by Celgard® 2325 separator (diameter = 3/4 inch (19 mm), thickness = 25 μm). After assembly, cells were rested for 10 h, followed by 3 formation cycles at 0.1C from 3 to 4.2 V. The charge profile consisted of galvanostatic charge with a 1C current, followed by a constant voltage step (4.2 V until 0.1C). The cells were discharged galvanostatically at 1C. All cells were run on Arbin high-precision cyclers. Electrochemical impedance spectroscopy was conducted with BioLogic SP-300 electrochemical workstation at a 1 mV AC amplitude and frequency ranging from 3 MHz to 300 mHz. Distribution relaxation time (DRT) methodology was employed to convert Nyquist plots from frequency domain to time domain. The open-access MATLAB GUI toolbox, called "DRTtools", which was developed by Francesco Ciucci's group, was employed to transform EIS spectrum acquired from EC-lab to DRT data.[39,40] The cycling temperature was maintained at 30 °C under a temperature-controlled incubator.

2.3 MnO_2–Li coin cells for temperature measurement

All MnO_2 cathodes were acquired from disassembled CR2032 3V coin cells purchased from Amazon Basics having a nominal capacity of 225 mAh. Li foil was used as anode, and the electrodes were separated by 250-μm glass fiber (Whatman®, GE) or Celgard® 2325 separator. The external current was applied by the BioLogic SP-300 electrochemical workstation. To measure the internal temperature from all three major components (namely, cathode, separator and anode) in a single cell, UCNPs were dispersed around the hole edges of glass fiber separator (hole diameter = 1/16 inch (0.16 cm)) and Li anode (hole diameter = 1/8 inch (0.32 cm)), respectively, and three layers were aligned in center to avoid short circuit.

2.4 Temperature calibration and measurements

Due to the large thickness (~3.2 mm) and unknown thermal resistance of the coin cells, temperature deviation may exist between the thermal stage and the coin cells. Therefore, temperature calibrations for UCNPs were conducted in separate samples of simpler and thinner structures designed to mimic the optical environment of the coin cell while providing a uniform temperature between the thermal stage and UCNPs. Such samples were fabricated as follows: substrate materials including MnO_2, glass fiber, Celgard®, and Li metal were sealed between two glass substrates (thickness 0.1 mm) after UCNP deposition of 3 μl with concentration of 20 mg ml^{-1}. A laser intensity of 1.3 kW cm^{-2} was applied and emission spectrum from UCNP was collected per second. A Kapton film was attached to one side of the glass to mimic the optical path of the modified coin cell. For each sample, we select five locations and measure at eight temperature points ranging from room temperature to 76 °C. After raising the temperature, we waited over 30 minutes to allow the thermal stage to reach a steady state. Fig. S1† shows the optical measurement setup for both temperature calibration and internal temperature measurement of coin cells. The thermocouple was attached to the back side of the stainless iron cell case of the modified cell using tape to perform *operando* monitoring of the external temperature evolution. The room where the internal temperature measurement was performed was controlled to ~19.5 °C.

2.5 Materials characterizations

The scanning electron microscopy (SEM) was conducted on a ZEISS Crossbeam 340 FIB-SEM system with an accelerating voltage of 7.5 kV. One minute of Au sputtering (15 mA, 200 mTorr) was applied to reduce charge accumulation effects. Transmittance of the Kapton film was acquired by the UV-Vis spectrometer (Thermo Fisher Scientific Evolution 300) with a scanning rate of 100 nm min^{-1}.

2.6 COMSOL simulation for optical window influence on coin cell temperature

Heat transfer simulations were performed using COMSOL. Heat generation is attributed solely to the cathode (MnO_2) instead of both electrodes, as Joule heating produced at the anode is negligible compared to that produced at the cathode due to the high internal electrical resistance of the cathode at high currents.[41] The Li anode is a fully dense metal with high electrical (~1.1×10^5 S cm^{-1}) conductivity.[42] MnO_2, on the other hand, is intrinsically less conductive (~10^{-5} to 10^{-6} S cm^{-1}); furthermore, it is assembled into a composite electrode structure with binder and conductive carbon additives, leading to high electrical contact resistances.[43] The thermal conductivity of the materials used in the simulation is summarized in Table S2.† The effective thermal conductivity of the glass fiber saturated with electrolyte, k_e is estimated by the model of thermal resistors in parallel:[44] $k_e = (1 - p) \times k_{separator} + p \times k_{electrolyte}$ where $k_{separator}$, $k_{electrolyte}$, and p represent the thermal conductivity of the electrolyte, glass fiber, and porosity of the glass fiber, respectively. As the thermal interface resistance is poorly understood but dominates the total thermal resistance, we estimate it based on limited previous studies.[8] Following prior reports that indicate 60% of the total resistance is due to thermal interface resistance, we first sum up the thermal resistances of all components. Then, we estimate the thermal interface resistances between the electrode and electrolyte, obtaining a value of 0.01 K m^2 W^{-1} for each interface. As delineated in the methods section, the optical path is established by creating perforations in the cell case, lithium metal, and glass fiber. The additional electrolyte is introduced to fill the perforations in the simulation to mimic the realistic modified coin cell structure. Fig. S4c and S4d† illustrate that the overall temperature rise in both the unmodified and modified cells remains consistent. We also noticed ~1.5 °C difference between the internal and external temperature in both cases. The negligible temperature variation between the modified and unmodified cases indicates that the changes to the coin cell structure do not affect the overall temperature rise or the temperature difference between the internal and external parts of the coin cell.

Published on 27 2568. Downloaded on 4/2/2569 17:04:26.

3. Results and discussion

3.1 Schematic representation of upconversion nanothermometry and custom electrochemical cell

Here, we illustrate that $NaYF_4:Yb^{3+},Er^{3+}$ UCNPs with well-understood temperature-dependent spectra[45,46] can be used for *operando* monitoring of internal temperature changes in operating coin cells. The custom-built microscopy and spectroscopy instrumentation is described in Fig. S1.† In this example, UCNPs are dispersed onto the surface of a conventional composite lithium-ion battery cathode, although in practice, they can be applied to any component that is optically accessible within the cell (demonstrated later). The cathode is then assembled with the other battery components in a coin cell. As illustrated in Fig. 1a, these components and coin cell case are modified with a small hole sealed with a Kapton film to provide an optical path to the UNCPs, enabling acquisition of temperature-dependent spectra and facilitating ratiometric luminescence thermometry. The transmittance spectrum of the Kapton® window used to seal the coin cell can be found in Fig. S2.† Specifically, the first band of emission in Fig. 1c is suppressed more than the second band due to the increasing transmission of the Kapton film over the wavelength range 500–600 nm, which results in a lower luminescence ratio value compared to previous work.[47]

The underlying photophysical mechanism is depicted in Fig. 1b. Upon excitation by a 976 nm laser, Yb^{3+} ions transfer energy to the Er^{3+} ions.[48] The Er^{3+} ions are excited to the $^4F_{7/2}$ state and subsequently non-radiatively decay to the $^2H_{11/2}$ and $^4S_{3/2}$ states, resulting in green emission. Thermalization between these two states is rapid relative to competing radiative and non-radiative depopulation rates, ensuring that their population ratio obeys the Boltzmann distribution, making their upconversion emissions around 540 nm and 525 nm temperature-dependent and suitable for ratiometric luminescence thermometry.[49] Fig. 1c shows two representative spectra of UCNPs on MnO_2 cathode materials at 20 and 76 °C, demonstrating an increase in the 525 nm emission band relative to the 540 nm emission with temperature. Further details on temperature calibration from these spectra will be discussed subsequently. Assuming ideal conditions, the spatial resolution of the thermometry technique is based on the laser spot size on the sample. It is calculated by $D = \lambda/(2 \times NA)$, where D is the spot size, λ is the excitation wavelength (976 nm), and NA is the numerical aperture of the objective (0.8). For this system, the ideal spatial resolution is 610 nm. Because the beam can distort due to interferences within the optical path (*e.g.* electrolyte and Kapton film window), the spatial resolution of the system can be fairly characterized as "sub-micrometer" (specified in Table S3†).

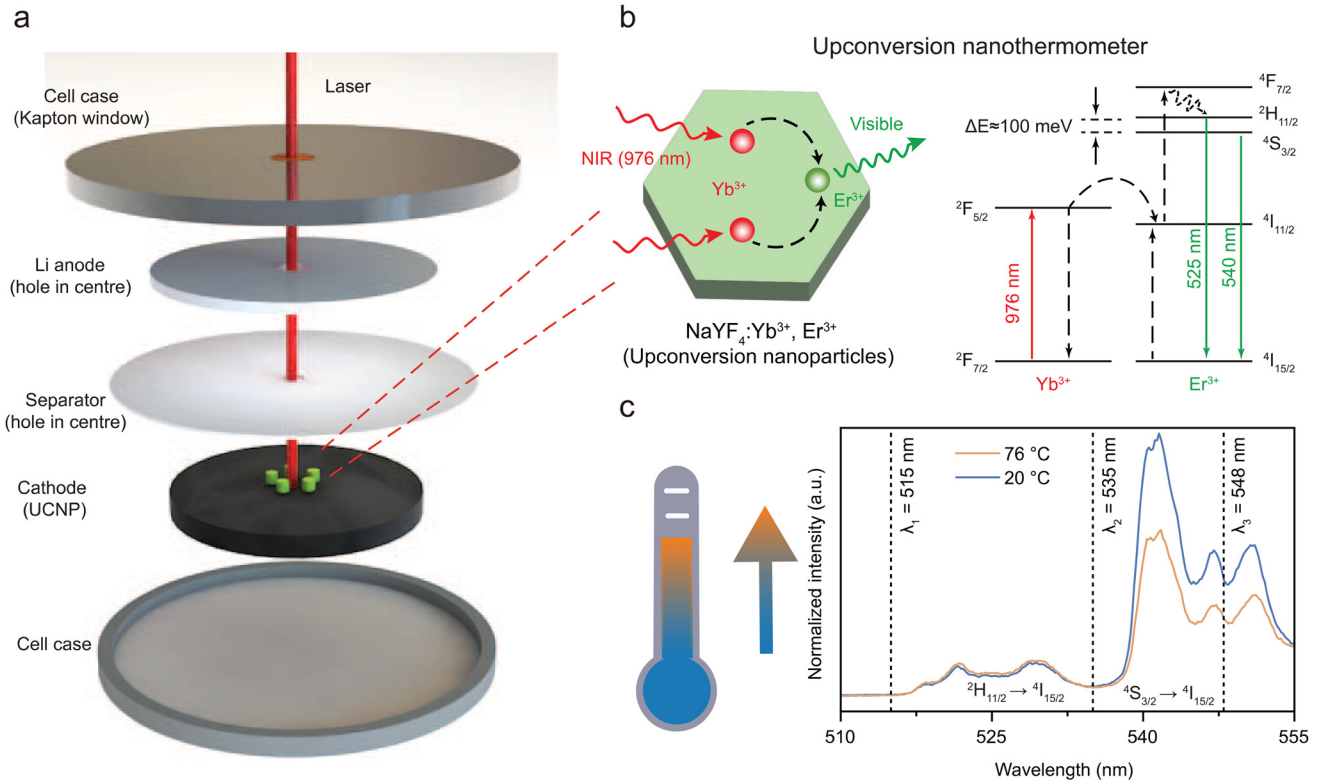

Fig. 1 Schematics of upconversion nanothermometry and custom coin cell for *in situ*, *operando* characterization. (a) Custom coin cell configuration, illustrating UCNPs applied to the cathode surface and optical path through the other cell components. (b) Photophysical mechanism for upconversion nanoparticles, and (c) luminescence spectra of UCNPs on MnO_2 cathode at 20 and 76 °C.

This journal is © The Royal Society of Chemistry 2025

Published on 27 2568. Downloaded on 4/2/2569 17:04:26.

3.2 Effect of UCNPs on cell electrochemistry and thermal processes

UCNPs were incorporated into lithium-ion battery half cells (excess Li metal) to investigate their effect on electrochemical processes within the cell. Lithium-ion battery coin cells were assembled as shown in Fig. 1a. Voltage profiles at 1C in Fig. 2a exhibit highly comparable charge and discharge plateaus after 50 cycles, with no indication of electrochemical side-reactions from the addition of UCNPs. The differential capacity analysis (dQ/dV) in Fig. S3a† shows one distinct anodic peak (3.77 *vs.* 3.81 V) attributed to phase transformation (*i.e.* $Ni^{2+} \leftrightarrow Ni^{3+} \leftrightarrow Ni^{4+}$ and $Co^{3+} \leftrightarrow Co^{4+}$) of NMC532 on both the baseline and UCNP coated cathode, with no additional peaks detected—suggesting that the rare-earth elements in UCNPs do not react with lithium.[50–52] The capacity retentions of the two cells over 50 cycles of galvanostatic cycling at a 1C rate are presented in Fig. 2b. The slight difference in capacity retentions is statistically insignificant, suggesting that the addition of UCNPs has a negligible effect on the cycling performance of rechargeable batteries. Although capacity loss was approximately 10% for both cells after 50 cycles, this is mainly due to the high rate (1C) and unoptimized carbonate electrolyte that led to irreversible interfacial reactions and Li loss during cycling. Furthermore, to evaluate the stability of UCNPs during cycling, emission spectra were collected before and after 50 cycles (Fig. S3b†). The unchanged peak positions and intensities support the chemical stability of UCNPs, reinforcing the reliability of the temperature measurements.

SEM characterization reveals the distribution of UCNPs on the NMC cathode (Fig. 2c). The low-magnification image shows the hierarchical "meatball"-like NMC active material particles surrounded by chain-like carbon black conductive additive and poly (vinylidene fluoride) (PVDF) binder. Individual UCNPs with diameters of tens of nanometers aggregate, forming clusters at the grain boundaries of the polycrystalline cathode active materials. To understand how the observed clusters of UCNPs on the cathode surface impact

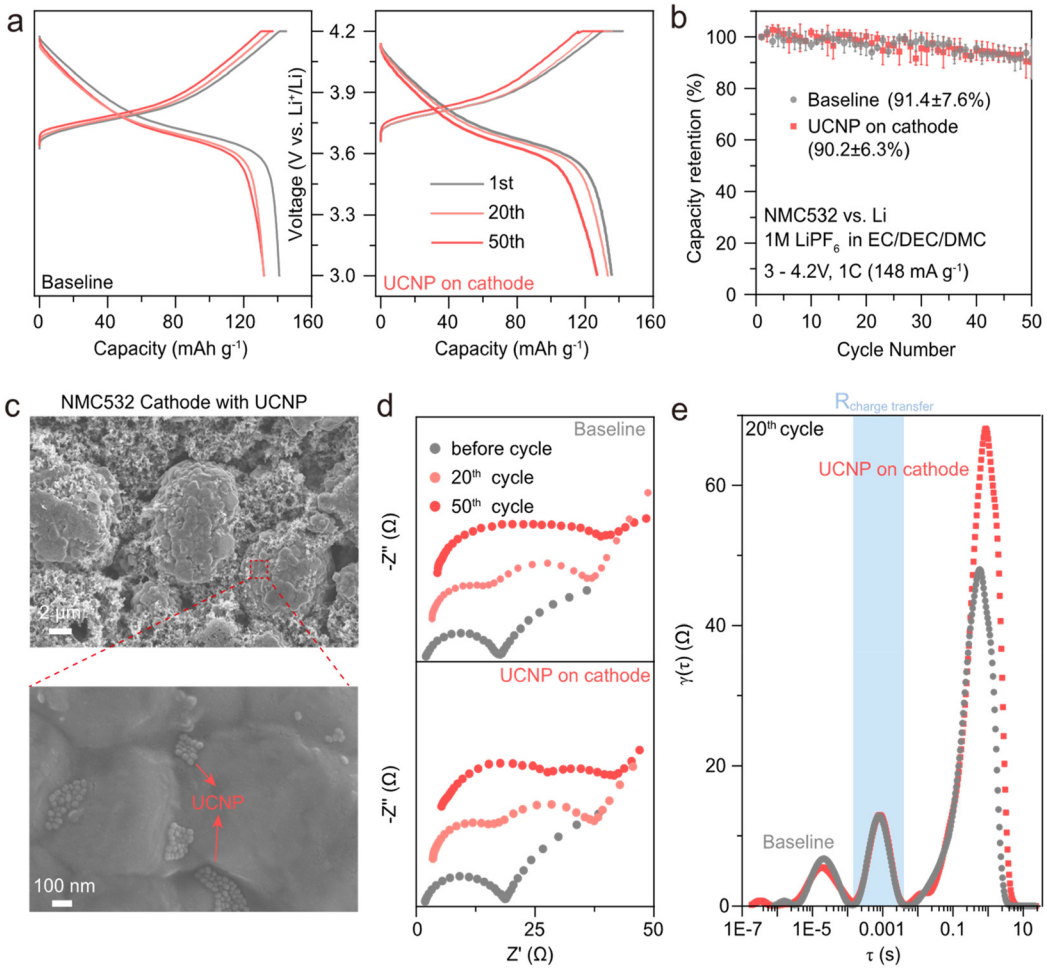

Fig. 2 Effect of UCNPs on performance of lithium-ion battery coin cells. (a) Voltage *vs.* capacity profiles with and without UCNPs applied to the cathode and (b) corresponding capacity retention *vs.* cycle number. The error bars represent the standard deviation of three replicate measurements. (c) Top-down SEM images of UCNPs on the NMC532 cathode. (d) Electrochemical impedance spectroscopy (EIS) spectrum of the coin cells after the 1st, 20th, and 50th cycle. (e) Distribution of relaxation time analysis of impedance spectra in panel (d). Cell parameters: NMC532 cathode, Li metal anode and 1 M $LiPF_6$ in EC/DEC/DMC electrolyte. Cycling parameters: 3 to 4.2 V at 1C current and 25 °C.

Published on 27 2568. Downloaded on 4/2/2569 17:04:26.

interfacial kinetics, electrochemical impedance spectroscopy characterization was employed. As the UCNP solution was applied uniformly over the electrode, this cluster morphology is expected to be representative of the entire electrode surface. Electrochemical impedance spectroscopy characterization was used to discriminate the effect of these observed UCNP clusters on the local charge transfer kinetics at the cathode interface and separately assess their impact from the global performance characterization of the cells (Fig. 2a and b). The baseline and NMC cathodes with UCNPs present similar total resistance before cycles and after 20 cycles, with resistance increasing to over 40 ohms and finally approaching 50 ohms after 50 cycles (Fig. 2d). The spectra consist of semicircles associated with the Li metal interface and cathode charge transfer resistance, with a low-frequency tail for solid diffusion inside electrodes. The progressively increasing resistance of both batteries (with and without UCNPs) is comparable and primarily attributed to the battery aging rather than the inclusion of UCNPs. As the UCNPs are affixed to the cathode surface, their effect on interfacial kinetics was assessed through quantification of the cathode charge transfer resistance (R_{CT}). The distribution of relaxation times (DRT) methodology was applied to straightforwardly compare R_{CT} as shown in Fig. 2e. By converting the frequency domain Nyquist plots (Fig. 2d) to time-based distributions, DRT offers valuable insights by deconvoluting highly overlapped electrochemical process to separate time domains (τ) without the necessity of fitting subjective equivalent circuits.[39,40,53] After 20 cycles, three major peaks are resolved and attributed to the solid electrolyte interphase (SEI) at the Li anode surface (τ = 10^{-5} to 10^{-4} s), charge transfer (10^{-4} to 10^{-2} s) on cathode surface, and solid state diffusion (10^{-2} to 10 s) in cathode.[54] The first and second peaks assigned to SEI and charge transfer, respectively, are comparable with or without UCNPs, implying that both Li anode and NMC cathode presented similar electrochemical interfacial behavior. The comparable R_{CT} of both cells further suggests that the UCNP clusters do not hinder the ion or electron transport process at the cathode interface (Fig. S4†).

Characterization of the internal temperatures using UCNP thermometry requires establishment of a clear optical path to the region of interest as depicted in Fig. 1a. To estimate the effect of these structural modifications on the temperature field, COMSOL finite-element simulations of the temperature fields were generated comparing the standard and modified cells (Fig. S5†). With a fixed power density assigned to the cathode, the spatial perturbation of temperature due to the structural modifications was found to be negligible, thereby validating the accuracy of the cell component temperatures measured by the UCNPs. Combined with electrochemical characterization of the NMC half cells, these results suggest that UCNP thermometry can be applied to lithium batteries with minimal impact on electrochemical and thermal behavior.

3.3 Temperature calibration of UCNPs

For *operando* characterization of the battery internal temperature, calibrations of UCNPs in contact with the various cell components are necessary to account for local environmental effects on the luminescence spectra and improve measurement accuracy. Commercial CR2032 MnO_2||Li coin cells were used for *operando* characterization because their superior capacity (225 mA h) relative to experimental lithium-ion battery half cells (~10–20 mA h) allows the use of larger current densities over reasonable experimental durations. Complete details of the calibration are provided in the ESI.† Fig. 3a and b reveal the distribution of the UNCPs on MnO_2 cathode and glass fiber separator, respectively. Again, the UCNPs cluster in morphological surface features of the components. SEM images of unmodified components without UCNPs can be found in Fig. S6.† UCNP distribution on the Li anode was not character-

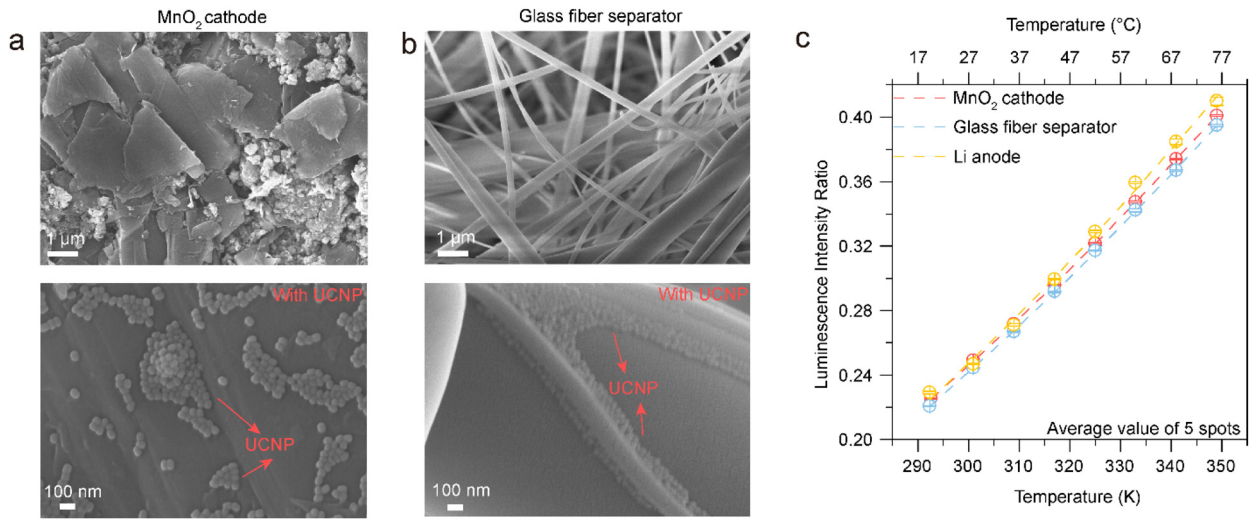

Fig. 3 Temperature calibration. SEM images of (a) MnO_2 cathode and (b) glass fiber separator with UCNPs. (c) The average luminescence intensity ratio calibration curve of UCNPs on the surface of MnO_2 cathode, glass fiber separator and Li anode.

 This journal is © The Royal Society of Chemistry 2025

Published on 27 2568. Downloaded on 4/2/2569 17:04:26.

ized because Li metal oxidizes due to the brief air exposure when transferring the Li to the SEM chamber, obscuring the nanoscopic UCNPs on the surface. The luminescence ratio r is defined as

$$\frac{\int_{\lambda_1}^{\lambda_2} I(\lambda)\mathrm{d}\lambda}{\int_{\lambda_2}^{\lambda_3} I(\lambda)\mathrm{d}\lambda} \equiv r = A\exp\left(-\frac{\Delta E}{k_B T}\right), \quad (1)$$

where $I(\lambda)$ represents the spectrum intensity, k_B is the Boltzmann constant, ΔE is the energy difference between the $^2H_{11/2}$ and $^4S_{3/2}$ states, and A is a constant related to radiative transition rates from these two thermally coupled states to $^4I_{15/2}$. The integration bounds are set as λ_1 = 515 nm, λ_2 = 535 nm and λ_3 = 548 nm to exclude the influence of emission beyond 548 nm from excited state-to-excited state transitions that results in artifacts in the ratiometric thermometry method applied here, which has been discussed extensively in prior work.[47,55,56] Fig. 3c shows the luminescence intensity ratio *versus* temperature calibration measured on MnO_2 (cathode), glass fiber (separator) and Li metal (anode); the average value of five different locations on each component defined the luminescence intensity ratio at each temperature. The dashed lines represent fits to eqn (1) and the fitted parameters A and ΔE are summarized in Table S1.† The calibrations are conducted at an excitation intensity of 1.3 kW cm^{-2}. The corresponding temperature-dependent luminescence spectra and intensity ratio used for the calibrations at various temperatures is shown in Fig. S7 and S8.† The fitted parameters for UCNPs on lithium metal differ slightly from those for UCNPs on the non-metallic cathode and separator, potentially due to photonic effects caused by metallic surfaces,[57] underscoring the necessity of conducting separate calibrations for UCNPs on different substrates. The calibration curves shown in Fig. S8† exhibit good uniformity across five different locations on each substrate with deviation <0.5 K, which is calculated by taking the standard deviation of converted temperatures using five calibration curves and one measured input ratio. This uniformity enables reliable internal temperature measurements with good temperature resolution. Other performance parameters such as the temporal resolution, spatial resolution, and temperature range of our method are summarized in Table S3.†

3.4 *Operando* internal temperature measurement

Primary MnO_2–Li commercial coin cells were assembled for *operando* monitoring of local temperatures of the internal cell components. Fig. 4a shows the internal/external temperature evolutions as a function of current, where the incident laser directly irradiated the surface of the MnO_2 cathode through holes in the cell case, Li anode and glass fiber separator. The first 6 min period was an open-circuit rest (zero current), which allowed assessment of the heating due to the incident laser power. Consistent temperature readouts (~19 °C) over the initial 6 min from the internal measurement of embedded UCNPs and external measurement of the thermocouple validate that laser heating is negligible under a laser power intensity of 1.3 kW cm^{-2}. This intensity is also at least an order of magnitude lower than what is commonly employed in single-UCNP thermometry.[56,58] As discussed previously, the expected spatial resolution of the temperature measurement on the cathode is sub-micrometer. After the initial 6 min, the cell was discharged at 10 mA for 15 min. The temperatures of the MnO_2 surface and exterior coin cell case both increased due to the heat generation, ultimately reaching 24.6 and 24.1 °C, respectively. An open circuit rest from 21 to 40 min allowed the cell to cool to room temperature. A higher current of 15 mA was then applied to generate more heat but was limited to a shorter discharge time (6 min), and the maximum internal MnO_2 and exterior case temperature were 24.6 and 23.7 °C, respectively. Ultimately, upon increasing the discharge current to 20 mA, the highest internal temperature (34.1 °C) of the cathode was measured with a maximum temperature difference of 2.3 °C between the cathode and external cell case.

To further demonstrate the characterization of internal temperatures of key components in a single Li cell, a primary MnO_2–Li cell with UCNPs dispersed on MnO_2 cathode, glass fiber separator, and Li anode simultaneously was assembled (Fig. 4b). The laser was first focused on the MnO_2 cathode while the cell was galvanostatically discharged at 15 mA, and the local internal temperature on the cathode rose to 24.3 °C after 6 min. The cell was allowed to rest under an open circuit to cool to room temperature, and the laser beam spot was refocused on the perimeter of the hole in the glass fiber separator. Under identical discharge parameters (15 mA for 6 min), the internal temperature slightly increased to 22.1 °C. After another open circuit rest to room temperature, the laser was moved to the perimeter of the hole in the Li anode, and the internal temperature rose to 22.9 °C after the same discharge protocol. The temperature increases are slightly different on the cathode, separator and anode under identical discharge profiles, possibly due to variations in the thermal environment of the cell from air convection and HVAC cycling in the laboratory or due to the evolution of internal thermal properties with repeated high current discharges. However, the excellent agreement between the external case and internal temperatures of all components during this proof-of-concept experiment validates the accuracy and versatility of the UCNP characterization approach.

Polyolefin separators (*e.g.* Celgard®) are the most common separator employed in commercial lithium ion batteries. The ability to characterize their temperature inside a battery is critical as they undergo critical thermally-induced failure mechanisms, such as softening and melting, leading to electrode contact and rapid discharge of thermal energy and exacerbating thermal runaways and battery fires. Thus, the suitability of UCNPs towards Celgard® separators was also investigated (Fig. 4c). The distribution of UCNPs on the surface of Celgard® is shown in Fig. S9,† and the details of the requisite temperature calibration are provided in Fig. S10.† The UCNP-loaded Celgard® separators were assembled into the commercial primary lithium cells, replacing the OEM glass fiber separators. Because Celgard® separators are an order of magnitude thinner than the glass fiber separators and contrib-

Published on 27 2568. Downloaded on 4/2/2569 17:04:26.

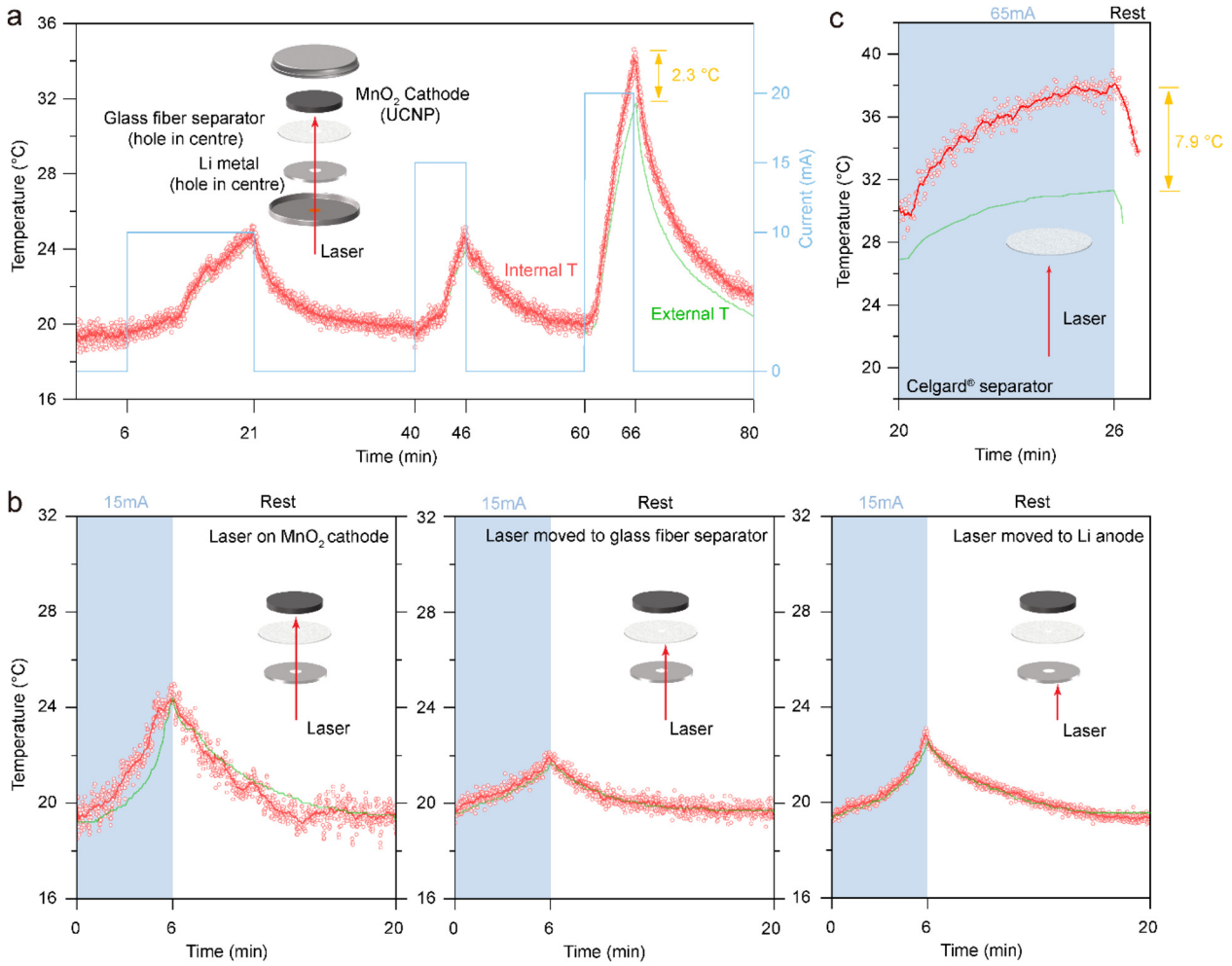

Fig. 4 *Operando* internal temperature measurement. (a) Temperature evolution of commercial coin cell (CR2032) with UCNPs on MnO_2 cathode for the corresponding galvanostatic cycling protocol (blue line). (b) At a fixed external current of 15 mA, the laser incidence was moved from the MnO_2 cathode, glass fiber separator, and Li anode in a single coin cell (CR2032). (c) Partial temperature evolution of coin cell (CR2032) with UCNPs on Celgard® separator with an external current at 65 mA for 6 min; the complete temperature profile can be found in Fig. S10.† Hollow red dots represent the measured raw internal temperature data and solid red lines are fitted to the data by averaging every 10 points. Green lines are external temperature data measured by a thermocouple attached to the coin cell case exterior.

ute less ohmic resistance, higher currents were applied to generate larger temperature differences – the full *operando* characterization profile is provided in Fig. S10.† At the highest current of 65 mA, the temperature of the Celgard® separator and external coin cell case increased to 39.0 and 31.1 °C, respectively, over six minutes as shown in Fig. 4c. The maximum temperature difference was 7.9 °C. Although Joule heat is dominating under the high current, these results show that the technique can yield internal temperatures from state-of-the-art lithium-ion battery materials, providing critical insight for battery thermal management.[41]

4. Conclusions

To the best of our knowledge, this work is the first to demonstrate the use of UCNPs embedded in each component of a coin cell for *operando* thermometry from the interior of the coin cell. We have shown that UCNPs are inert within the electrochemical cell and do not adversely affect cell performance. A key advantage of this approach is the ability to embed UCNPs on distinct cell components (*e.g.*, cathode, anode, and separator), allowing spatially-resolved temperature measurements from within the cell. Applied to a commercial Li primary cell, a temperature difference of 2.3 °C was observed on the MnO_2 cathode under a discharge current of 20 mA. In a further modified cell, wherein the relatively thick glass fiber separator is replaced with state-of-the-art polyolefin Celgard®, a maximum temperature difference of 7.9 °C between the separator and cell case was measured when discharged at 65 mA. The key capabilities offered by UCNPs include high spatial (sub-micron) and temporal (seconds) resolution with relatively minor disruptions to the electrochemical cell, suggesting that the technique can be readily extended to state-

 This journal is © The Royal Society of Chemistry 2025

of-the-art, large format, fast-charge lithium ion batteries to provide critical understanding of thermal behavior and internal cell temperatures for improved battery safety.

Author contributions

Fei Hu: writing – original draft, methodology, investigation, formal analysis, data curation, conceptualization. Ziyang Ye: writing – original draft, investigation, formal analysis, data curation, conceptualization. Andrea D. Pickel: writing – review & editing, validation, supervision, methodology, funding acquisition, conceptualization. Wyatt E. Tenhaeff: writing – review & editing, validation, supervision, methodology, funding acquisition, conceptualization.

Data availability

All data supporting the findings of this study are included in the article or the ESI.†

Conflicts of interest

There are no conflicts to declare.

Acknowledgements

Fei Hu acknowledges and expresses his appreciation from the Kwang-Yu and Lee-Chien Wang graduate fellowship and Elon Huntington Hooker dissertation fellowship. The authors would also like to thank Professor Alexander Shestopalov and Zonglun Li for providing the UV-vis spectrometer for characterization and thank Argonne National Laboratory for offering NMC532 cathodes. The NMC532 electrodes were produced at the U.S. Department of Energy's (DOE) CAMP (Cell Analysis, Modeling and Prototyping) Facility. The CAMP Facility is fully supported by the DOE Vehicle Technologies Office (VTO). Furthermore, the authors acknowledge the valuable open-source MATLAB-based DRT tool from Professor Francesco Ciucci's group from Hong Kong University of Science and Technology.

References

1 Y. Liu, Y. Zhu and Y. Cui, *Nat. Energy*, 2019, **4**, 540–550.
2 C.-Y. Wang, T. Liu, X.-G. Yang, S. Ge, N. V. Stanley, E. S. Rountree, Y. Leng and B. D. McCarthy, *Nature*, 2022, **611**, 485–490.
3 X. Feng, D. Ren, X. He and M. Ouyang, *Joule*, 2020, **4**, 743–770.
4 Y. Zeng, D. Chalise, S. D. Lubner, S. Kaur and R. S. Prasher, *Energy Storage Mater.*, 2021, **41**, 264–288.
5 Z. Xiao, C. Liu, T. Zhao, Y. Kuang, B. Yin, R. Yuan and L. Song, *J. Electrochem. Soc.*, 2023, **170**, 057517.
6 A. Jinasena, L. Spitthoff, M. S. Wahl, J. J. Lamb, P. R. Shearing, A. H. Strømman and O. S. Burheim, *Front. Chem. Eng.*, 2022, **4**, 804704.
7 Z. Wei, J. Zhao, H. He, G. Ding, H. Cui and L. Liu, *J. Power Sources*, 2021, **489**, 229462.
8 S. D. Lubner, S. Kaur, Y. Fu, V. Battaglia and R. S. Prasher, *J. Appl. Phys.*, 2020, **127**, 105104.
9 H. Szeto, V. Kumar and Y. Zhu, *ACS Energy Lett.*, 2024, **9**, 4218–4224.
10 K. Yu, W. Chen, D. Deng, Q. Wu and J. Hao, *Sensors*, 2024, **24**, 2057.
11 L. Raijmakers, D. Danilov, R.-A. Eichel and P. Notten, *Appl. Energy*, 2019, **240**, 918–945.
12 D. Li, L. Wang, C. Duan, Q. Li and K. Wang, *Int. J. Energy Res.*, 2022, **46**, 10372–10388.
13 S. Ma, M. Jiang, P. Tao, C. Song, J. Wu, J. Wang, T. Deng and W. Shang, *Prog. Nat. Sci.: Mater. Int.*, 2018, **28**, 653–666.
14 C.-Y. Lee, S.-J. Lee, Y.-M. Hung, C.-T. Hsieh, Y.-M. Chang, Y.-T. Huang and J.-T. Lin, *Sens. Actuators, A*, 2017, **253**, 59–68.
15 B. Li, M. H. Parekh, R. A. Adams, T. E. Adams, C. T. Love, V. G. Pol and V. Tomar, *Sci. Rep.*, 2019, **9**, 13255.
16 A. Raghavan, P. Kiesel, L. W. Sommer, J. Schwartz, A. Lochbaum, A. Hegyi, A. Schuh, K. Arakaki, B. Saha and A. Ganguli, *J. Power Sources*, 2017, **341**, 466–473.
17 C.-Y. Lee, S.-M. Chuang, S.-J. Lee, I.-M. Hung, C.-T. Hsieh, Y.-M. Chang and Y.-P. Huang, *Sens. Actuators, A*, 2015, **232**, 214–222.
18 A. Ganguli, B. Saha, A. Raghavan, P. Kiesel, K. Arakaki, A. Schuh, J. Schwartz, A. Hegyi, L. W. Sommer and A. Lochbaum, *J. Power Sources*, 2017, **341**, 474–482.
19 S. Novais, M. Nascimento, L. Grande, M. F. Domingues, P. Antunes, N. Alberto, C. Leitão, R. Oliveira, S. Koch and G. T. Kim, *Sensors*, 2016, **16**, 1394.
20 J. Huang, L. A. Blanquer, C. Gervillié and J.-M. Tarascon, *J. Electrochem. Soc.*, 2021, **168**, 060520.
21 C. Gervillié-Mouravieff, L. A. Blanquer, C. Alphen, J. Huang and J.-M. Tarascon, *J. Power Sources*, 2023, **580**, 233268.
22 M. S. Wahl, L. Spitthoff, H. I. Muri, A. Jinasena, O. S. Burheim and J. J. Lamb, *Energies*, 2021, **14**, 3617.
23 A. Olgo, S. Genies, R. Franchi, C. Septet, Q. Jacquet, Q. Berrod, R. Palm, P. Chenevier, E. Villemin and C. Villevieille, *Nat. Commun.*, 2024, **15**, 10258.
24 Y. Cheng, S. Zhao, G. Shen, S. Zhang and P. Yao, *ACS Omega*, 2024, **9**, 19517–19524.
25 T. Heenan, I. Mombrini, A. Llewellyn, S. Checchia, C. Tan, M. Johnson, A. Jnawali, G. Garbarino, R. Jervis and D. Brett, *Nature*, 2023, **617**, 507–512.
26 X. Yu, Z. Feng, Y. Ren, D. Henn, Z. Wu, K. An, B. Wu, C. Fau, C. Li and S. J. Harris, *J. Electrochem. Soc.*, 2018, **165**, A1578.
27 Y. Zhu, J. Xie, A. Pei, B. Liu, Y. Wu, D. Lin, J. Li, H. Wang, H. Chen, J. Xu, A. Yang, C.-L. Wu, H. Wang, W. Chen and Y. Cui, *Nat. Commun.*, 2019, **10**, 2067.

Published on 27 2568. Downloaded on 4/2/2569 17:04:26.

Published on 27 2568. Downloaded on 4/2/2569 17:04:26.

28 S. Faure, N. Mille, S. S. Kale, J. M. Asensio, J. Marbaix, P. Farger, D. Stoian, W. van Beek, P.-F. Fazzini and K. Soulantica, *J. Phys. Chem. C*, 2020, **124**, 22259–22265.
29 G. Viera, S. Huet and L. Boufendi, *J. Appl. Phys.*, 2001, **90**, 4175–4183.
30 F. Huang, K. T. Yue, P. Tan, S.-L. Zhang, Z. Shi, X. Zhou and Z. Gu, *J. Appl. Phys.*, 1998, **84**, 4022–4024.
31 J. P. Schmidt, S. Arnold, A. Loges, D. Werner, T. Wetzel and E. Ivers-Tiffée, *J. Power Sources*, 2013, **243**, 110–117.
32 R. Srinivasan, B. G. Carkhuff, M. H. Butler and A. C. Baisden, *Electrochim. Acta*, 2011, **56**, 6198–6204.
33 N. S. Spinner, C. T. Love, S. L. Rose-Pehrsson and S. G. Tuttle, *Electrochim. Acta*, 2015, **174**, 488–493.
34 R. R. Richardson, P. T. Ireland and D. A. Howey, *J. Power Sources*, 2014, **265**, 254–261.
35 S. Chamola and S. Ahmad, *Next Energy*, 2025, **7**, 100239.
36 H. Li, F. Wei, Y. Li, M. Yu, Y. Zhang, L. Liu and Z. Liu, *J. Mater. Chem. C*, 2021, **9**, 14757–14765.
37 Y. Wang, Q. Zhang, C. Yang and Z. Xia, *Small*, 2025, 2501651.
38 Y. Wang, Q. Zhang, C. Yang and Z. Xia, *Adv. Mater.*, 2024, **36**, 2401057.
39 T. H. Wan, M. Saccoccio, C. Chen and F. Ciucci, *Electrochim. Acta*, 2015, **184**, 483–499.
40 M. B. Effat and F. Ciucci, *Electrochim. Acta*, 2017, **247**, 1117–1129.
41 S. Du, Y. Lai, L. Ai, L. Ai, Y. Cheng, Y. Tang and M. Jia, *Appl. Therm. Eng.*, 2017, **121**, 501–510.
42 Technical data for Lithium, **https://periodictable.com/Elements/003/data.html**.
43 J.-G. Wang, *Supercapacitor Design and Applications*, 2016.
44 J. Wang, J. K. Carson, M. F. North and D. J. Cleland, *Int. J. Heat Mass Transfer*, 2006, **49**, 3075–3083.
45 C. D. Brites, R. Marin, M. Suta, A. N. Carneiro Neto, E. Ximendes, D. Jaque and L. D. Carlos, *Adv. Mater.*, 2023, **35**, 2302749.
46 B. Harrington, Z. Ye, L. Signor and A. D. Pickel, *ACS Nanosci. Au*, 2023, **4**, 30–61.
47 A. D. Pickel, A. Teitelboim, E. M. Chan, N. J. Borys, P. J. Schuck and C. Dames, *Nat. Commun.*, 2018, **9**, 4907.
48 J. D. Kilbane, E. M. Chan, C. Monachon, N. J. Borys, E. S. Levy, A. D. Pickel, J. J. Urban, P. J. Schuck and C. Dames, *Nanoscale*, 2016, **8**, 11611–11616.
49 S. Zhou, K. Deng, X. Wei, G. Jiang, C. Duan, Y. Chen and M. Yin, *Opt. Commun.*, 2013, **291**, 138–142.
50 S.-B. Son, D. Robertson, Y. Tsai, S. Trask, A. Dunlop and I. Bloom, *J. Electrochem. Soc.*, 2020, **167**, 160508.
51 L. Zhang, J. Jiang and W. Zhang, *Energies*, 2017, **10**, 1147.
52 M. Dixit, M. Kosa, O. S. Lavi, B. Markovsky, D. Aurbach and D. T. Major, *Phys. Chem. Chem. Phys.*, 2016, **18**, 6799–6812.
53 M. Nohl, G. Raut, S. E. Wolf, T. Duyster, L. Dittrich, I. Vinke, R.-A. Eichel and L. De Haart, *ECS Trans.*, 2021, **103**, 1403.
54 Y. Lu, C.-Z. Zhao, J.-Q. Huang and Q. Zhang, *Joule*, 2022, **6**, 1172–1198.
55 X. Xia, A. Volpi, J. Y. D. Roh, M. C. De Siena, D. R. Gamelin, M. P. Hehlen and P. J. Pauzauskie, *J. Lumin.*, 2021, **236**, 118006.
56 P. Rodríguez-Sevilla, Y. Zhang, P. Haro-González, F. Sanz-Rodríguez, F. Jaque, J. G. Solé, X. Liu and D. Jaque, *Adv. Mater.*, 2016, **28**, 2421–2426.
57 T. P. Van Swieten, T. Van Omme, D. J. Van Den Heuvel, S. J. Vonk, R. G. Spruit, F. Meirer, H. H. P. Garza, B. M. Weckhuysen, A. Meijerink and F. T. Rabouw, *ACS Appl. Nano Mater.*, 2021, **4**, 4208–4215.
58 K. Suresh, K. Monisha, A. Bankapur, S. K. Rao, S. Mutalik and S. D. George, *Anal. Chim. Acta*, 2023, **1273**, 341530.

This journal is © The Royal Society of Chemistry 2025